SCIENTIFIC REPORTS

OPEN

Electrically tunable valley polarization in Weyl semimetals with tilted energy dispersion

Received: 5 October 2018
Accepted: 18 February 2019
Published online: 14 March 2019

Can Yesilyurt[1], Zhuo Bin Siu[1], Seng Ghee Tan[2], Gengchiau Liang[1], Shengyuan A. Yang[3] & Mansoor B. A. Jalil[1]

Tunneling transport across electrical potential barriers in Weyl semimetals with tilted energy dispersion is investigated. We report that the electrons around different valleys experience opposite direction refractions at the barrier interface when the energy dispersion is tilted along one of the transverse directions. Chirality dependent refractions at the barrier interface polarize the Weyl fermions in angle-space according to their valley index. A real magnetic barrier configuration is used to select allowed transmission angles, which results in electrically controllable and switchable valley polarization. Our findings may pave the way for experimental investigation of valley polarization, as well as valleytronic and electron optic applications in Weyl semimetals.

Charge carriers in crystal lattices may carry a valley isospin degree of freedom, in addition to their real spin. Recent theoretical and experimental works[1–4] have predicted and demonstrated the existence of valley-dependent transport features in condensed matter systems, in which valley polarization has been demonstrated by using magnetic fields[5–8], line defects[9], and optical helicity[10]. A considerable amount of effort has been made to achieve valley dependent tunneling in condensed matter systems. One possible avenue is by applying a uniaxial strain to induce a relative shift of the two valleys at the corners of the hexagonal unit cell of the reciprocal lattice. As a result, the Fermi surfaces experience a shift in k-space, causing the electrons around different valleys to experience refractions in opposite directions at the interface between the strained and unstrained regions[11]. Although the gradient of uniaxial strain results in the angular separation of electron trajectories according to the valley index, this in itself would not give rise to valley-polarized conductance since the contributions of both valleys to the overall conductance are still identical. To induce a valley-polarized transport, one needs to break the angular symmetry of transmission profile by means of transverse Lorentz displacement[12–17], which may be achieved by applying a magnetic barrier. This forms the basis of various valley transport or filter applications in graphene and silicene[12–17]. However, such an approach does not provide a convenient mechanism to control or modulate the valley transport dynamically. This is because the modulation would entail either a change of the direction of the applied strain or switching of the magnetization direction of the magnetic material. Another way to achieve valley polarized tunneling is via the valley-dependent substrate-induced band gap, together with the application of gate voltage and inhomogenous magnetic field profile[18,19]. In this approach, the lifting of valley degeneracy is strongly related to the valley-dependent band structure induced by a particular substrate (e.g., h-BN). Due to the fixed value of the Dirac band gap, this may entail precise tuning of parameters, such as the Fermi energy and applied gate voltage to achieve a finite valley polarization. Here, we show that valley dependent tunneling can be controlled solely by means of an electrical potential applied to a region of Weyl semimetal with tilted energy dispersion. Theoretically, the proposed valley polarization approach is not restrictive in that it does not require a precise range of parameter values. The mechanisms used to lift the valley degeneracy (i.e., electrical potential barrier) and to select the desired valley transmission (i.e., magnetic barrier) are both tunable. Besides, the previously reported methods for generating valley polarization have been applied to the specific context of graphene. These methods may be material-dependent, e.g. strain, or substrate induced band gap may not be directly applicable

[1]Electrical and Computer Engineering, National University of Singapore, Singapore, 117576, Republic of Singapore. [2]Department of Optoelectric Physics, Chinese Culture University, Taipei, 11114, Taiwan. [3]Research Laboratory for Quantum Materials, Singapore University of Technology and Design, Singapore, 487372, Singapore. Correspondence and requests for materials should be addressed to C.Y. (email: can-yesilyurt@hotmail.com) or M.B.A.J. (email: elembaj@nus.edu.sg)

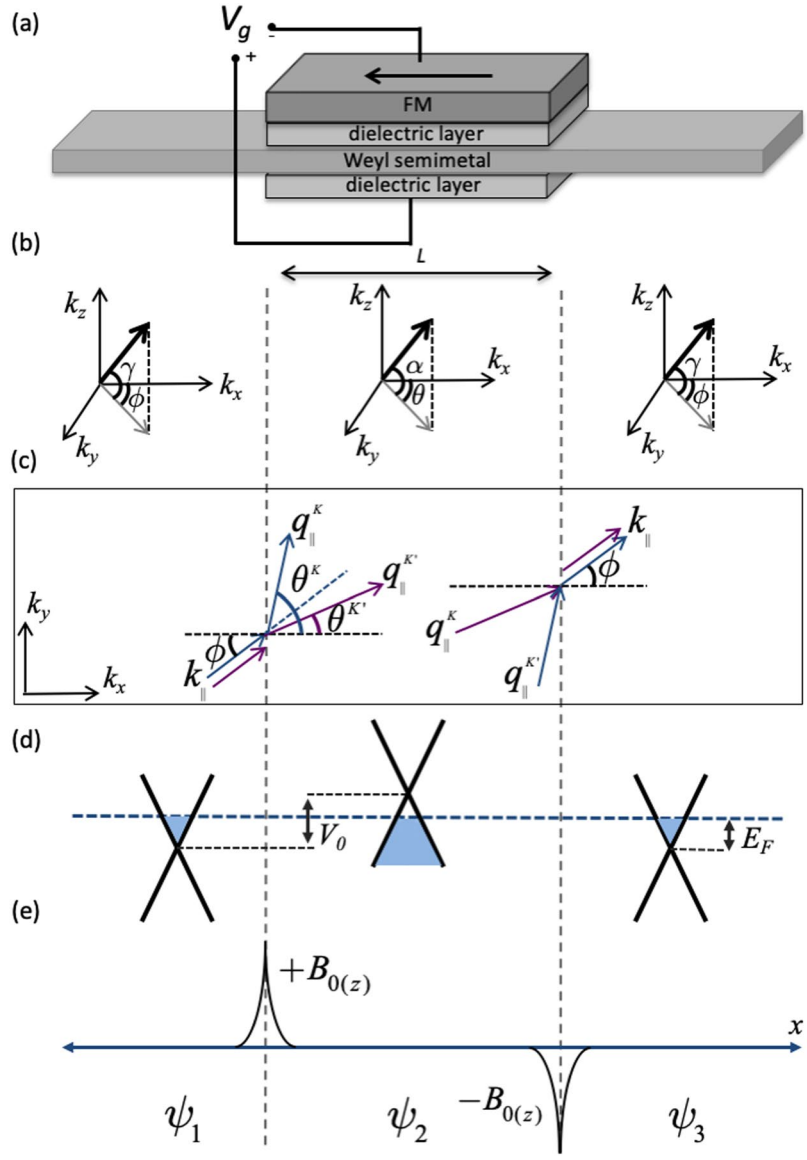

Figure 1. (**a**) Weyl semimetal with one-dimensional rectangular electrical potential and magnetic barrier induced by ferromagnetic (FM) layer deposited on the central region. The black arrow shows the magnetization direction of the FM layer. (**b**) Shows the electron propagation angles outside and within the barrier region. (**c**) Illustrates the valley dependent refractions at the barrier interfaces. (**d** and **e**) Demonstrate the effect of applied electric potential on the central region and magnetic field induced by the FM layer respectively.

to three-dimensional Weyl and Dirac semimetals. Therefore, additionally our work proposes the realization of valleytronic applications in a new material platform, i.e., Weyl semimetals.

It has been previously shown that Weyl fermions that encounter a potential barrier experience an anomalous transverse momentum shift along the direction of the tilt[20,21]. We focus on the simplest Weyl semimetal case where the time reversal symmetry is broken, which allows the presence of a single pair of Weyl nodes related by the inversion symmetry. Later we will comment on the validity of our calculations in the systems consisting of multiple pairs of Weyl nodes. The valley resolved angular dependence of transmission probability shows that the electrons around different valleys experience deflections along different directions at the barrier interface as illustrated in the Fig. 1(c) for an electron incident with momentum $k_\parallel$. We consider an additional magnetic barrier configuration applied to the central region to select a particular angle range allowed for transmission, which results in valley-polarized conductance. In this letter, as an example, the magnetic barrier is generated by a FM layer on the top of the barrier region as illustrated in Fig. 1(a). While the role of the magnetic barrier is to extract a particular valley polarization, it plays no part in tuning the valley polarization (the magnetic barrier strength is kept constant). We will show that modulation of the valley polarization can be achieved by tuning the applied gate voltage, i.e., by changing the voltage, the valley isospin that contributes to the conduction can be switched.

Model

The electronic states in Weyl semimetals consist of two different types, i.e., Weyl nodes separated in k-space and Fermi arc states connecting the projection of two Weyl nodes on a surface[22–27]. The contribution of the Fermi arc states to the tunneling conductance is negligible as shown in a Dirac semimetal Na_3Bi[28], as well as the following sections. Total transmission of the system can be calculated by taking into account only Weyl nodes as considered in various previous works[29–33]. The robustness of the Weyl semimetal case strongly depends on the k-space distance of the Weyl nodes, i.e., the length of the Fermi arc. It has been shown that the Fermi arc length can be tunable[34], and specific materials (e.g. TA_3S_2) having robust widely separated Weyl nodes have been predicted[35]. In terms of electron transport, these developments would lead to low intervalley scattering effects as long as transmission direction is chosen properly (i.e., discussed in the following sections). Weyl fermion comprises of two bands with linear dispersion along three dimensions, which are degenerate at a Weyl point. Since Weyl nodes usually occur at generic k-points in the Brillouin zone with lower symmetry, Weyl fermions generally possess tilted energy dispersion (as seen in TaP, and NbAs). A Weyl fermion can be described by a general low-energy Hamiltonian such as

$$H = V_0 + \sum_i \hbar k_i \tau \, (v_i \sigma^i + w_i), \tag{1}$$

where σ's are Pauli matrixes, and V_0 is external electrical potential. In general, the velocities v's may be asymmetric in three-dimension, and their sign ($\tau = \pm$) carry the chirality of Weyl nodes. However, we assume symmetric velocities equal to $v_F = 10^6\, m/s$ in the rest of the manuscript. The dispersion of Weyl fermion can be tilted along all three directions, and the strength of the tilt is denoted by w_i. Based on the proposed approach, the tilt direction must be aligned along one of the transverse directions (y-direction in this letter unless otherwise stated). Therefore, the tilt vector is defined as $w = (0,\ \chi w_y,\ 0)$, where $\chi = \pm$ according to the valley index assuming the case where the energy dispersion is tilted along opposite directions in different valleys. We consider ballistic tunneling transmission along the x-direction and the incident angles are characterized by γ (the angle between k and the x-y plane) and ϕ (the azimuthal angle with respect to the x-axis), as shown in Fig. 1(b). Two inequivalent valleys separated in k-space are represented by K and K'. The wave vectors are described by

$$\begin{aligned} k_x &= k_F \cos\gamma \cos\phi, \\ k_y &= k_F \cos\gamma \sin\phi, \\ k_z &= k_F \sin\gamma, \end{aligned} \tag{2}$$

where the Fermi wave-vector

$$k_F = (E_F - V_0)/\hbar(v_F + \chi w_y \cos\gamma \sin\phi). \tag{3}$$

We consider a one-dimensional rectangular potential barrier, which is described by $V_{(x)} = V_0[\Theta(x) - \Theta(x - L)]$, as illustrated in Fig. 1(d). From the practical point of view, such a potential barrier can be induced in Weyl semimetals either by changing the carrier concentration locally by means of electrical gates, and/or doping with alkali metal atoms[36,37]. Electrostatic gates have been commonly used to tune carrier concentration in two-dimensional materials. Recent experimental works show that dynamic tuning of the carrier concentration is achievable in three-dimensional materials as shown in Dirac semimetal Cd_3As_2[36] and Weyl semimetal WTe_2[38]. The electrostatic gating requires very thin material structure, whose thickness is restricted by the range of the screening effect. Another requirement is that the sample must reach sufficient thickness to allow formation of Weyl nodes in the bulk. For instance, gate bias tuning of the carrier concentration of bulk states has been demonstrated in 50-nm thick Cd_3As_2[36] and 14-nm thick WTe_2[38].

The FM layer placed on the central region induces two spike-like magnetic fringe fields at the barrier boundaries, as illustrated in Fig. 1(e). Note that a thin film dielectric layer is deposited between the Weyl semimetal and FM layer to avoid induced magnetization in the former due to the proximity effect. To derive an analytical solution of the problem, we first assume the simplified magnetic barrier[12–15,39–41] which can be approximately described by two asymmetric delta magnetic fields $B_{z(x)} = B_0[\delta(x) - \delta(x - L)]$ along the z-direction. Later, we will discuss a more realistic magnetic field profile, which shows that the shape of the magnetic field profile does not play a vital role in the proposed method. By the choice of the Landau gauge, the delta magnetic fields give rise to a piecewise constant magnetic vector (gauge) potential $\overrightarrow{A_B} = B_0 l_B[\Theta(x) - \Theta(x - L)]\hat{y}$. The transverse wave vector experience a shift such that $k_y \rightarrow k_y + eA_B/\hbar$ within the barrier region. The same magnetic barrier structure can be achieved by various methods and configurations such as two FM strips with asymmetric perpendicular magnetic anisotropy deposited on the barrier boundaries[42–48], as well as superconductor film fabricated with the desired pattern on the Weyl semimetal and applying uniform magnetic field[45,49,50]. By considering both electrical and magnetic barriers, the momentum along the transmission direction within the barrier is given by

$$q_x = \frac{\sqrt{-\hbar^2 v_F^2((k_y + \delta k_y)^2 + k_z^2) + (-E_F + V_0 + \hbar\chi w_y (k_y + \delta k_y))^2}}{\hbar v_F}, \tag{4}$$

where $\delta k_y = eA_B/\hbar$. Due to the conservation of energy and transverse momentum, electrons experience refractions at the barrier interface, and the propagation angles of the transmitted electrons are given by $\theta = \tan^{-1}\left(\frac{k_y}{q_x}\right)$ and $\alpha = \tan^{-1}\left(\frac{k_z}{q_x}\cos\theta\right)$ within the barrier region, as illustrated in Fig. 1(b). Solving the Hamiltonian in Eq. 1, the wave functions of incident, propagated and transmitted electrons are found as

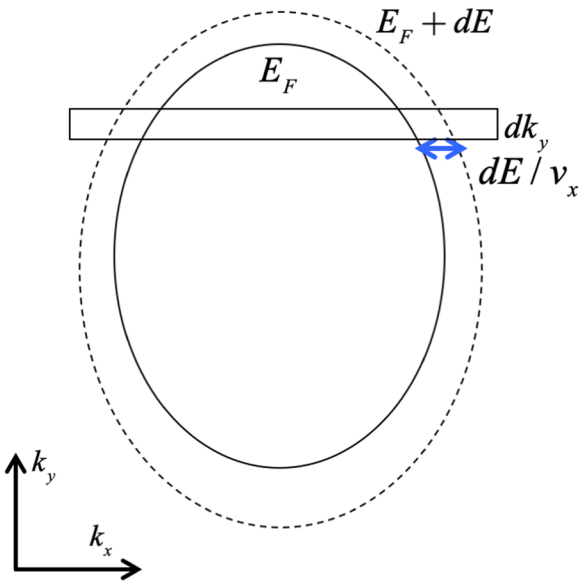

Figure 2. The solid ellipse represents a Fermi surface; and the dotted ellipse shows $E_F + dE$.

$$\psi_{\pm} \equiv \frac{1}{\sqrt{2}} e^{i\vec{k}\cdot\vec{r}} \begin{pmatrix} 1 \\ e^{i\phi} \sec\gamma\,(\eta + \sin\gamma) \end{pmatrix} \equiv \begin{pmatrix} \psi_a \\ \psi_b^{\eta} \end{pmatrix} \tag{5}$$

The wave function is composed of two spinor components ψ_a and ψ_b^{η}, where $\eta = \text{sign}(E_F - V_0)$ is the band index. To analyze the angular dependence of electron tunneling we calculate the transmission probability across the system by matching the top and bottom components of the wave functions at the barrier interfaces. $T^{K}_{(\phi,\gamma)}$ and $T^{K'}_{(\phi,\gamma)}$ denote the transmission probability of electrons around K and K' respectively. Transmission between K and K' is neglected based on the analysis presented in the sections below. We assume equilibrium system, where the source and drain are at the same chemical potential, and thus the Fermi level assumed to be level throughout. To derive the analytical solution, we have neglected the scattering mechanisms in our calculation. However, it has been shown that the angular refractions of electrons (which is a key component of our proposal) and the resultant transmission profile in tilted Weyl systems are robust against weak disorders[20]. The Fermi surface of the tilted Weyl fermion is not a perfect sphere, which must be taken into account in the conductance integral. The infinitesimal element of the elliptical Fermi surface per unit variation of the coordinates ϕ and γ is found as

$$dS_{FS} = \frac{E_F^2 \cos\gamma \sqrt{v_F^2 + (\chi w_y)^2 + 2v_F \chi w_y \cos\gamma \sin\phi}}{\hbar^2 (v_F + \chi w_y \cos\gamma \sin\phi)^3} d\phi d\gamma. \tag{6}$$

The total valley dependent conductance can be calculated considering anisotropic band dispersion based on Landauer-Büttiker formalism. In systems with two or three dimensions, the conserved transverse momentum can be treated as a parameter with a given value. To calculate the transmission, one can sweep through the range of the transverse momentum covered by the source Fermi surface and integrate over the transmission contribution at each value of the transverse momentum. This is illustrated by the diagram (Fig. 2), which shows a two-dimensional system on the xy plane where the interface is along the x direction and k_y is conserved.

For simplicity we assume $\hbar = 1$ in the following derivations. At each given value of k_y, the k-space area between the $E = E_F$ and $E = E_F + dE$ surface is $\frac{1}{v_x} dE dk_y$. In the Landauer-Büttiker formalism $dE = eV_B$ where the V_B is the applied bias between the source and drain. The number of states per unit real-space area per dk_y is then $\frac{1}{(2\pi)^2}\frac{1}{v_x} eV_B$. Denoting the transmission at each value of k_y, $T(k_y)$ the drain current for each state is $\frac{e}{L} T(k_y) v_x^d(k_y)$, and the total current would then be given by

$$I/(eV_B) = \int dk_y \frac{eW}{(2\pi)^2} \frac{v_x^d(k_y)}{v_x^s(dk_y)} T(k_y) \tag{7}$$

where W is the width of the system. The above integration is over the Equal Energy Contours (EECs) between the Fermi surface and the EEC at $E_F + eV_B$ where v_x is positive. This is the shaded area in panel (a) of Fig. 3 where the infinitesimal area element consists of horizontal strips. The panel (b) in Fig. 3 shows the integration over the incident angle $d\phi$. In the limit that dE goes to zero, the shaded areas in (a) and (b) are identical. The infinitesimal area element in (b) is $k_F(\phi) d\phi dE/v$.

In our system, the coordinates(ϕ, γ) are defined as

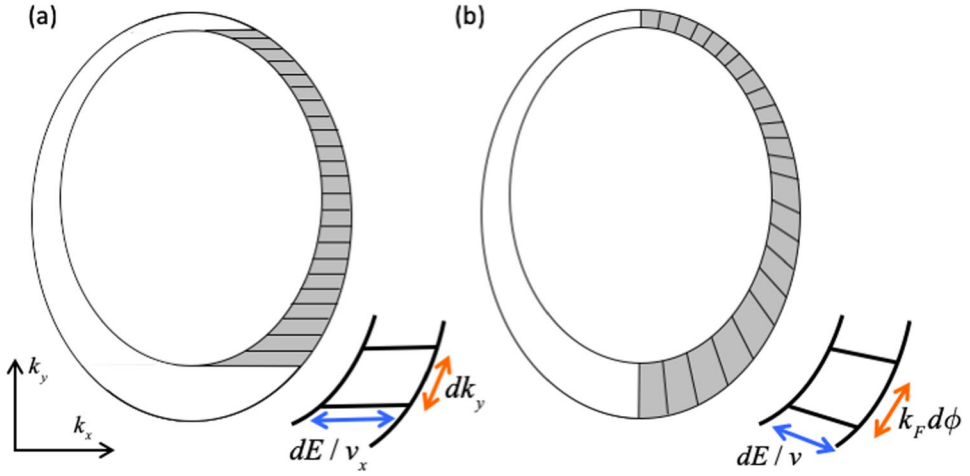

Figure 3. (**a**) Shows the integration over dk_y where the dimensions of the infinitesimal element are dk_y and $\frac{dE}{v_x}$. (**b**) Shows the integration over ϕ where the dimensions of the infinitesimal element are $k_F(\phi)d\phi$ and $\frac{dE}{v}$.

$$\begin{aligned} x &= k_F\cos(\gamma)\cos(\phi) \\ y &= k_F\cos(\gamma)\sin(\phi) \\ z &= k_F\sin(\gamma) \end{aligned} \tag{8}$$

Thus, the 3-dimensional analog of the Eq. 7 would then be

$$I/(eV_B) = \int\int_{FS} dk_y dk_z \frac{eA}{(2\pi)^3}\frac{v_x^d(k_y, k_z)}{v_x^s(k_y, k_z)}T(k_y) \tag{9}$$

where the subscript FS stresses the fact that the k_y and k_z values are to be chosen from points lying on the Fermi surface only. The above equation can be re-written as follows in terms of ϕ and γ.

$$I/(eV_B) = \int\int dS_{FS}\frac{eA}{(2\pi)^3}\frac{v_x^d}{v}T(\phi, \gamma) \tag{10}$$

In the above, note that the density of the states is related to $1/v$ instead of $1/v_x$. The infinitesimal area element per unit variation of ϕ and γ is

$$dS_{FS} = \frac{E_F^2\cos\gamma\sqrt{v_F^2 + (\chi w_y)^2 + 2v_F\chi w_y\cos\gamma\sin\phi}}{\hbar^2(v_F + \chi w_y\cos\gamma\sin\phi)^3}d\phi d\gamma. \tag{11}$$

The velocity operators are defined as $\hat{v}_x = v_F\hat{\sigma}_x, \hat{v}_y = v_F\hat{\sigma}_y + \chi w_y\hat{I}_\sigma, \hat{v}_z = v_F\hat{\sigma}_z$. Their corresponding expectation values of the velocity operators are given by

$$\begin{aligned} \langle\hat{v}_x\rangle &= v_F\cos(\gamma)\cos(\phi) \\ \langle\hat{v}_y\rangle &= v_F\cos(\gamma)\sin(\phi) + \chi w_y \\ \langle\hat{v}_z\rangle &= v_F\sin(\gamma) \\ v &= \sqrt{\langle\hat{v}_x\rangle^2 + \langle\hat{v}_y\rangle^2 + \langle\hat{v}_z\rangle^2} \end{aligned} \tag{12}$$

Assuming identical source and drain and restoring the $\hbar$, the conductance can be found as

$$G = G_0\int\int d\phi d\gamma \frac{\cos^2(\gamma)\cos(\phi)}{\left(1 + \frac{\chi w_y}{v_F}\cos(\gamma)\cos(\phi)\right)^3}T(\phi, \gamma) \tag{13}$$

where $G_0 = \frac{e^2E_F^2A}{(2\pi)^3\hbar^3v_F^2}$ is the quantum conductance, the integral being dimensionless. Finally, we define the valley polarization (e.g., for valley K) $P_K = (G_K - G_{K'})/(G_K + G_{K'})$.

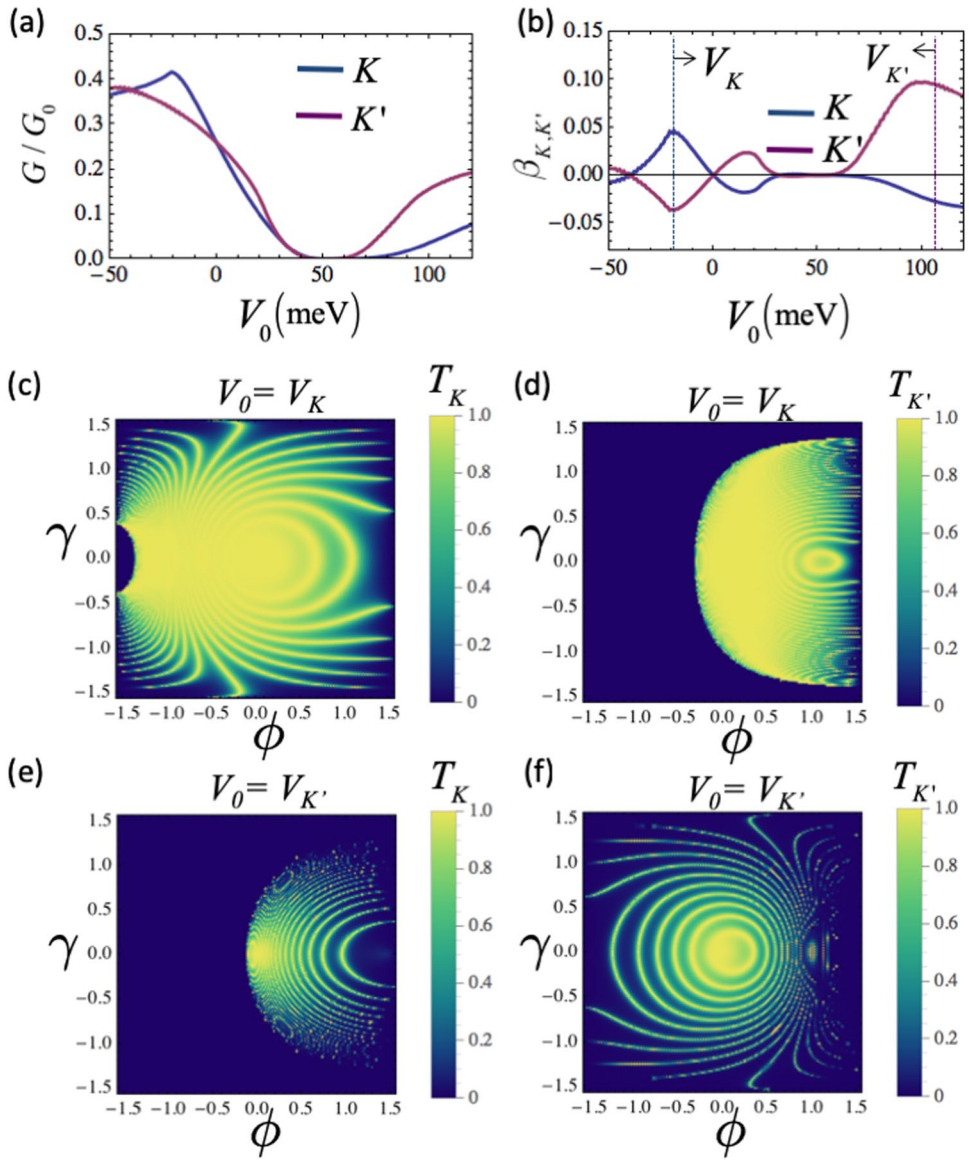

Figure 4. Valley resolved tunneling profile of Weyl electrons around two distinct valleys K and K'. The normalized tunneling conductance of K and K' is shown in (**a**), where the valleys exhibit different tunneling profiles in the case of varying external electrical potential V_0. The difference between the conductance profile of K and K' gives rise to valley-polarized conductance whose magnitude can be defined by $\beta_{K,K'}$ as shown in (**b**). At two chosen external potentials V_K and $V_{K'}$ [denoted by doted lines in (**b**)] which yield a high effective polarization $\beta_{K,K'}$ for the K and K' valley, respectively, the angular dependence of tunneling probability for both valleys is shown in (**c**–**f**). The tilt velocity $w_y/v_F = \chi 0.4$, the Fermi energy $E_F = 50$ meV, barrier length $L = 900$ nm, magnetic field $B_{z(x)} = 2$ T, and the conductance is in unit of G_0 for all configurations.

Results and Discussions

Valley-dependent conductance. The analytical derivation of valley dependent conductance (Eq. 13) allows us to analyze the whole conductance profile of the system for varying applied potential barrier height. The Fig. 4 shows the valley-dependent conductance profile of the system. The angular dependence of the transmission profiles of each valley at $V_0 = V_{K(K')}$ are shown in (c-f). The total conductance shown in (a) is calculated by considering continuous dispersion along all three directions. We observed that the highest valley polarization $P_{K(K')}$ occurs in the conductance gap region (i.e. $40 < V_0 < 60$ meV). However, this would be of little physical utility since the conductance of both valleys is negligibly low. Therefore, it is useful to introduce an effective valley polarization factor $\beta_{K(K')} = P_{K(K')} \times G_{K(K')}$ in order to evaluate the optimal conditions for high valley polarization and high conductance simultaneously. In Fig. 4(b and d), we consider the $\beta_{K(K')}$ factor for an exemplary device configuration where $B_0 = 2$ T, $E_F = 50$ meV, $w_y/v_F = \chi 0.4$ and found that the effective valley polarization can be switched and its magnitude controlled by tuning the potential barrier height V_0. Numerically, the high polarization of K' can be selected by setting $V_0 \approx 110$ meV which is denoted by $V_{K'}$ in Fig. 4(d). For the K valley, high polarization

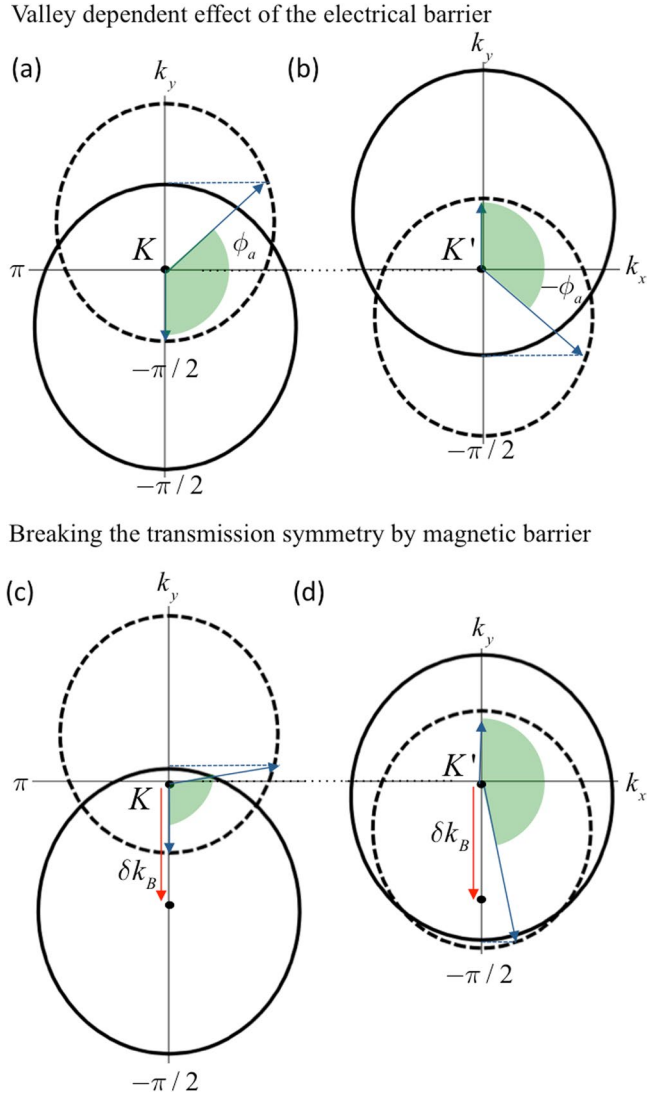

Figure 5. The dashed and solid-lined circles represent the Fermi surfaces of the first and second regions shown in Fig. 1 respectively. The conservation of transverse wave vector k_y limits the allowed transmission range in angle-space in the case of external electrical and magnetic potentials. K and K' are two inequivalent valleys which possess opposite chirality and opposite direction tilt ($w_y/v_F = \chi 0.4$) along the y-axis. (**a** and **b**) Illustrate that the applied electrical potential ($V_0 = 110\,\text{meV}$) gives rise to a valley dependent momentum shift, causing the valley dependent refraction and reflections at the barrier interface. (**c** and **d**) Demonstrate the further effect of external delta-magnetic field ($B_{0(z)} = 2\,\text{T}$) induced by FM layer on the central region, causing the contraction (at K) and extension to all possible angles in the forward direction (at K') of the allowed transmission range (denoted by the shaded angles). The Fermi energy $E_F = 50\,\text{meV}$.

occurs at $V_0 \approx -20\,\text{meV}$. At these voltage values V_K and $V_{K'}$, the inequivalent transmission profile can be clearly seen by analyzing the valley resolved angular dependence of transmission probability $T_{\phi,\gamma}^{K(K')}$, as shown in Fig. 2(c–f). The applied potential V_K combined with the effect of magnetic barrier suppresses the electron transmission for both valleys. However, the electrons around K' possess much more restricted allowed transmission angle range compared to the electrons around K (see Fig. 4(c and d)). On the other hand, the applied voltage $V_{K'}$ allows limited angle range for transmission at K, while the barrier allows transmission across almost the whole incident angle range at K', as shown in Fig. 4(e and f). This result indicates that the obtained valley polarization originates from electro-optical mechanisms, i.e., the refractions and reflections at the barrier interface.

Fermi surface orientation. To investigate the origins of the valley dependent tunneling shown above, we focus on the Fermi surface structure of the system at the barrier interface. The conservation of energy, momentum and chirality determines the ballistic electron transmission at the barrier interface. Therefore, one can predict the allowed incident angles that lead to high transmission by analyzing the matching of the Fermi surface and spin alignment at the barrier interface. In Fig. 5, the solid-lined (dashed) circle represents the Fermi surface in the presence (absence) of applied electrical potential $V_0 = V_{K'} = 110\,\text{meV}$, which is the barrier height for high $\beta_{K'}$.

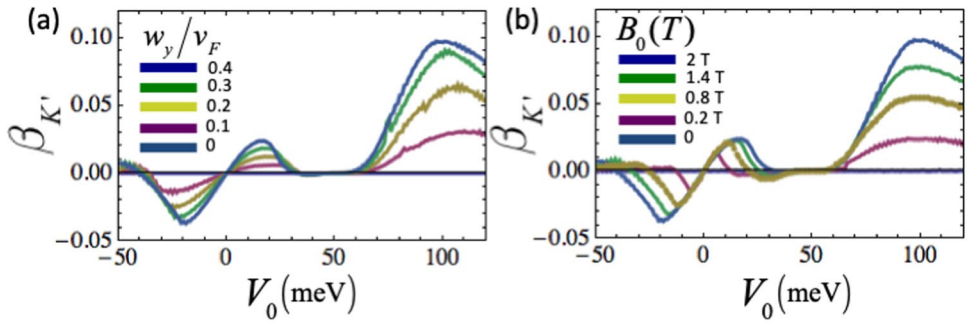

Figure 6. The effect of tilt strength and applied magnetic barrier on the polarization of K'. (**a**) Shows the $\beta_{K'}$ for different tilt strength, where $B_{0(z)} = 2\,\mathrm{T}$, (**b**) shows the $\beta_{K'}$ for different strength of applied magnetic barrier, where $w_y/v_F = \chi 0.4$. The Fermi energy $E_F = 50\,\mathrm{meV}$, and barrier length $L = 900\,\mathrm{nm}$ for all configurations.

Due to the opposite direction tilt of the Weyl nodes at K and K', the Fermi surfaces shift to opposite transverse directions as shown in Fig. 5(a and b). At K, the wave vector along transmission direction within the barrier, q_x becomes imaginary for the electrons whose incident angle is between $\pi/2$ and ϕ_a. On the other hand, this forbidden angle range is between $-\phi_a$ and $-\pi/2$ for the electrons around K'. This means that the electrons experience opposite direction deflections at the barrier interface according to their valley index. The magnetic barrier also causes a very similar shift of the Fermi surfaces. However, the effect of the magnetic barrier is valley-independent, which creates the same direction transverse shift for both valleys by means of transverse Lorentz displacement. As shown in Fig. 5(c and d), this additional one-way shift constricts the allowed angle range at K, while it widens the allowed range at K'. That remarkably shows that the barrier selectively reflects the incident electrons according to their respective valley index, causing the valley-polarized tunneling at the barrier interface. Note that the allowed range shown by shaded angles in Fig. 5 does not mean that all the incident angles in this range have high transmission since the tunneling at the barrier interface also requires the matching of the spin or pseudo-spin alignment. As can be seen in Fig. 4(c and d), tunneling transmission occurs between Weyl nodes with the same chirality in the case $V_0 = V_K$, causing the perfect matching of spin alignment; thus the transmission profile is only determined by the conservation of transverse momentum. However, Klein tunneling (chiral tunneling) transmission occurs in the case of $V_0 = V_{K'}$ since $V_{K'} > E_F$, which causes the different pattern of perfect transmission angles due to the different spin alignment of electron and hole states, as seen in Fig. 4(e and f).

To analyze the mechanisms that generate the valley-polarized transmission, we focus on the tilt strength of the Weyl nodes and applied magnetic barrier strength. As shown in Fig. 6(a), the valley polarization highly depends on the tilt strength that generates the valley-dependent transverse shift at the barrier interface. Note that this anomalous momentum shift is caused by the combined effect of the electrical potential and tilted band structure. The presence of only one of these factors would not lift the valley degeneracy. This combined effect lifts the valley degeneracy and separates the electrons in the two valleys in angle-space. However, the contribution of the both valleys to the overall conduction would still be the same, leading to zero valley polarization in conductance. We require the use of magnetic barrier to cause a valley-selective electro-magnetic effect at the barrier interface. Thus, the strength of the valley-polarization of the conductance will be dependent on the magnetic field strength as well, as shown in Fig. 6(b).

Realistic magnetic barrier. The magnetic barrier in our proposed system would only affect the electron momentum by means of fringe fields induced by the magnetization of the FM layer, and not via the induced exchange proximity effect. In the schematic diagram of the proposed system shown in Fig. 1, there is a dielectric layer placed between the Weyl semimetal and the FM layer. Hence the overlap between the wave functions of the FM layer and the Weyl semimetal which gives rise to the exchange proximity effect is effectively suppressed if the separation distance (dielectric thickness) is more than a few nanometers. However, the fringe fields induced by the magnetized FM layer would be effective along the device thickness. Here, we will delve deeper into the physics of the magnetic barrier structure and provide a detailed quantitative analysis based on a more realistic model. To calculate a more realistic magnetic barrier, we have considered the following magnetic field profile, which is consistent with the experimental results[48]:

$$B_z(x) = \frac{\mu_0 M_s}{4} \ln\left(\frac{x^2 + z^2}{(z + D)^2 + x^2}\right). \tag{14}$$

In the above, M_s is the saturation magnetization of FM layer, z is the thickness of the dielectric layer between FM layer and Weyl semimetal, and D is the thickness of the FM layer.

Based on the above equation, the FM layer on top of the Weyl semimetal induces two asymmetric spike-like magnetic fields at the edges, which is plotted in Fig. 7(a). The magnetic field strength at the peak reduces with increasing distance along z-direction, where the different colors represents different values of z. In addition to the change in the maximum value of the magnetic field strength, the field profile also spreads out over a wider extent in x. We note that the $\int B_x dx$ is constant at all depth z even though the peak value $B_{max}(z)$ reduces along z (see

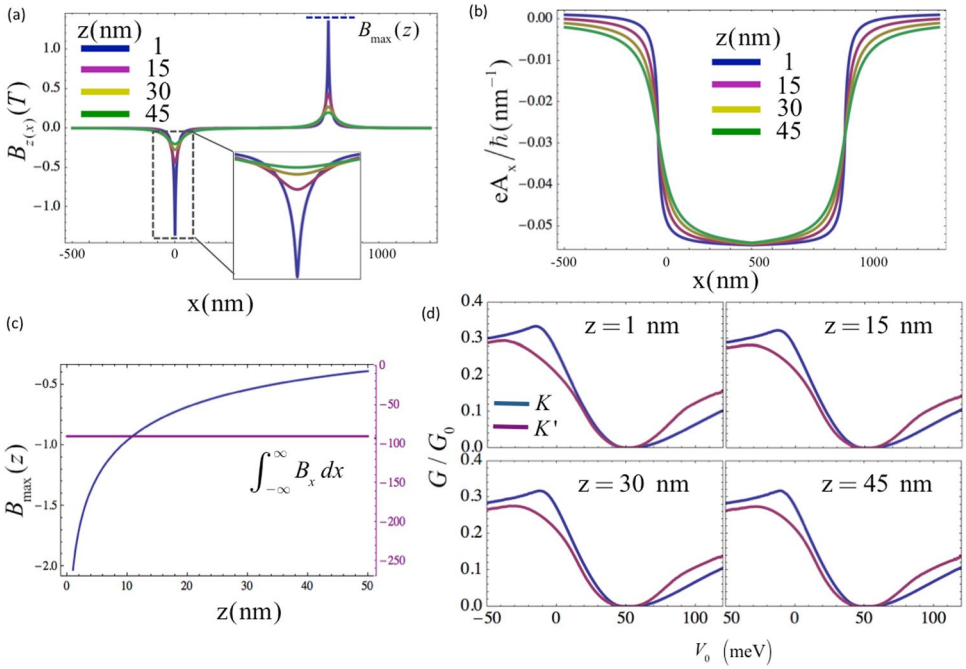

Figure 7. Realistic magnetic barrier configuration. (**a**) Shows magnetic field profile with two asymmetric peaks, induced at the edges of the FM layer shown in Fig. 1. Different colors represent the field profile at different points in the *z*-direction. (**c**) Shows the shift of the k_y due to the gauge potential A_x induced by the magnetic fields shown in (**a**). The maximum magnetic field strength $B_{max}(z)$ shown in (**a**) reduces with increasing distance along *z*, of which characteristic calculated for continuous distance in (**c**), while the integration of the magnetic field over *x* is constant as shown at the right axis in (**c**). Since the maximum height of the A_x does not depend on the field profile, the valley resolved conductance shows very similar profiles at varying depth of the proposed device, as shown in (**d**).

Fig. 7(c)). Note that the maximum height of the A_x does not depend on the $B_{max}(z)$ but the integral $\int B_{(x)}dx$. The proposed valley filtering method depends primarily on the Fermi surface overlap, and hence the maximum height of the A_x rather than the specific profile of A_x over different depth *z*. Thus, we envisage that the variation of the magnetic field strength along *z* would not have a strong influence on the valley dependent conductance of the system. To verify this, we perform numerical simulation by applying the realistic magnetic barrier profiles as shown in Fig. 7(a and b) and obtain the conductance profile of the system by considering different depths along *z*. The transmission probability is obtained by dividing the whole device into short segments where the magnetic gauge potential is spatially varying along *x*, and applying the transfer matrix method (ref.[51]). The conductance is calculated by using Eq. 13. The results shown in Fig. 7(d) reveal that the valley dependent conductance is highly robust against variation in the magnetic field profile along both *x* and *z*. For comparison, the saturation magnetization of the FM layer is set to the value that induces the same gauge potential height with that considered in Fig. 4. The conductance profiles in (d) are quite consistent with the result [Fig. 4(a)] obtained by considering a square shape gauge potential as described above, and which can be calculated analytically by the wave-function matching method.

In our model, the ferromagnetic (FM) layer magnetization is the in-plane direction. In the case of out-of-plane magnetization, there would be an approximately square shape B-field profile effective within the barrier region adjacent to the FM layer. This would generate a linearly increasing gauge potential profile in the barrier region, which is distinct from the square shape gauge profile shown in Fig. 7(b). In such case, there would still be non-zero valley polarization as the presence of valley dependent refractions does not depend on the specific B-field profile.

Ferromagnetic materials with high remanence and large bulk saturation magnetization would be appropriate in order to enhance the edge magnetic field and achieve high valley polarization. In previous experimental setups that possess similar magnetic barrier structures (see ref.[42]), dysprosium has been selected as the FM material due to this attribute. Following ref.[42], one can set the thickness of the FM layer to 300 nm, which gives rise to 3.75 T bulk saturation magnetization.

As for the dielectric layer, it should be made as thin as possible to achieve a strong magnetic field with a sharp field profile, but it must be more than a few atomic layers in thickness in order to avoid magnetic proximity effect[52–54]. The upper limit is the thickness where the spread of B-field is larger than the half of the barrier length. A suitable range of thickness of the dielectric layer would approximately be between 1 nm and 45 nm, as analyzed in Fig. 7(a).

Tuning the valley-polarization by gated potential barrier. One of the advantages of the proposed valley filter function is that its operation is not restricted to some specific parameter range. Theoretically, the

application of electrical barrier in tilted band structures causes a transverse momentum shift at the Fermi level and this shift is generally valley dependent. Similarly, any magnetic field along a particular direction, regardless of its strength or profile would break the angular symmetry of transmission by means of transverse Lorentz displacement. Thus, as can be seen from the Fig. 4(a and c), non-zero valley polarization can be achieved at any arbitrary applied gate voltage. However, the strength of the polarization can indeed be optimized by tuning the value of the gate voltage. As depicted in Fig. 1(d), the K and K' valley polarization can be optimized by setting the gate voltage at V_K and $V_{K'}$. These optimal voltage values are dependent on the applied magnetic field, which is tunable, as well as the intrinsic Fermi level which can be set by, e.g., alkali metal doping[37]. We believe that given the flexible parameter configuration for the operation of the proposed system, the generated valley polarization could be readily observed. Based on the parameter set demonstrated in Fig. 4, we require a change of the electrical potential of approximately 100 meV in order to switch the polarization between the two valleys. Such a change of potential can be achieved in a realistic system. For instance, let us consider gating by means of solid electrolytes[36] which is experimentally conducted in Cd_3As_2. The electron and hole densities have been tuned to values on the order of $10^{12}\,cm^{-2}$, where a change of Fermi level in excees 100 meV, i.e., between 143–254 meV, was achieved under an applied gate voltage change of 0 to 12 V, based on experimentally observed Shubnikov-de Haas oscillations[36]. A similar experiment also confirmed that the carrier density rises up to values on the order of $10^{12}\,cm^{-2}$ by application of gate voltage in WTe_2[55].

Effect of the finite device thickness on the valley polarization. Thus far, we assumed the condition where the finite thickness along z-direction is much larger than the Fermi wavelength λ_F. This allows us to use the continuum treatment without considering the quantization of k. However, having a small finite thickness may be a crucial factor if one requires the use of gated potential barriers due to the short range screening effect. Therefore, in this part, we consider the case where the system has a finite thickness along one of the directions and calculate the valley dependent conductance.

In this calculation, we apply the generic model (Eq. 15) that describes two Weyl nodes located at $k_x = k_y = 0$, $k_z = \pm\Delta k_z/2$, where Δk_z is the k-space distance between the two nodes.

$$H = \varepsilon_0 + \begin{pmatrix} M(\mathbf{k}) & Ak_+ \\ Ak_- & -M(\mathbf{k}) \end{pmatrix} \tag{15}$$

In the above, $\varepsilon_0 = C_0 + C_1k_z^2 + C_2(k_x^2 + k_y^2)$, $M(k) = -M_0 + M_1k_z^2 + M_2(k_x^2 + k_y^2)$ and $k_\pm = k_x \pm ik_y$. Since the parameters, i.e., A, C_i, and M_i are material-specific; we take the example of Na_3Bi_2, except C_1 which is modified to match the tilt velocity of our system for comparison with the analytical result presented.

Based on the requirements of the proposed valley filter, we chose the transmission direction along y-direction in this example, where the k_z is a good quantum number. The finite thickness d_x along the x-direction leads to sub-band dependent mass due to the quantization of k_x such that $\langle k_x^2\rangle_n \approx \frac{n\pi}{d_x}$, where $n = 1, 2, \ldots$. In order to obtain the eigenspectrum, the Schrodinger equation can be expanded in the basis of the $\langle x|\psi\rangle = \sqrt{2/d_x}\cos(n\pi x/d_x)$ infinite quantum well eigenstates and diagonalizing the resultant matrix (a more detailed explanations has been presented in refs[28,56,57]). The energy dispersion and quantized sub-bands of a system consisting of two Weyl nodes are shown in Fig. 8(a). The band structure also holds in the Dirac semimetal case with degenerate spins without coupling[58,59]. Therefore, the proposed valley filter is not restricted to Weyl semimetals and it can be also realized in Dirac semimetals with tilted energy dispersion. As shown in Fig. 8(a), the Weyl nodes exhibit tilted characteristic along the z-direction, which results in elliptical Fermi surfaces. When the energy shifts, the mismatch occurs between Fermi surfaces in the source and the drain regions, as shown in the illustration in Fig. 5. The conductance profile of a system depicted in Fig. 1, which consists of a 900-nm central barrier region sandwiched between the semi-infinite source and drain regions, is calculated numerically by matching of the wave functions at the barrier interfaces. A magnetic barrier is applied to the central region having the same profile as that described in Fig. 1. As plotted in Fig. 8(b), there is an imbalance in the conductance profiles of K and K' due to the combined effect of the electrical potential and the magnetic field. In the region between $V_0 \simeq -5$ meV and $V_0 \simeq 25$ meV, the conductance of K is higher than K'. This region largely coincides with the homogeneous junction case (p-p*-p). On the other hand, the conductance of K' is higher than K in the remaining range, which mostly coincides with heterogeneous junction case (p-n-p). This result is in close agreement with the results obtained earlier by the continuum treatment (Fig. 4) where the finite thickness d_x is much larger than the Fermi wavelength λ_F, and hence the quantization of k is ignored.

Detection of the generated valley polarization. Valleytronic applications have been reported in graphene-based structures, and various detection schemes have been presented for detecting the valley current in such systems. It has been experimentally shown in graphene systems with broken inversion symmetry, that valley-polarized current may cause inverse valley Hall effect that can be measured as a transverse voltage drop[2,60,61]. Alternatively, superconducting contacts can be used to detect valley polarized current based on Andreev reflection in systems where the valleys are related by time-reversal symmetry[62]. These schemes may be adapted for Weyl semimetal materials where the inversion symmetry is broken, while time-reversal symmetry is preserved.

Besides, the valley-polarized current can also be detected in our present scheme by including a second barrier in series with the first (similar to that shown in ref.[63]). Using the wave functions, and energy dispersion derived previously, the tunneling transmission can be calculated by the matching of the wave functions in the five regions at their respective barrier interfaces. The transmission probability is calculated numerically by the transfer matrix method. The (second) barrier that is used for detection must be set to a configuration where only one valley is

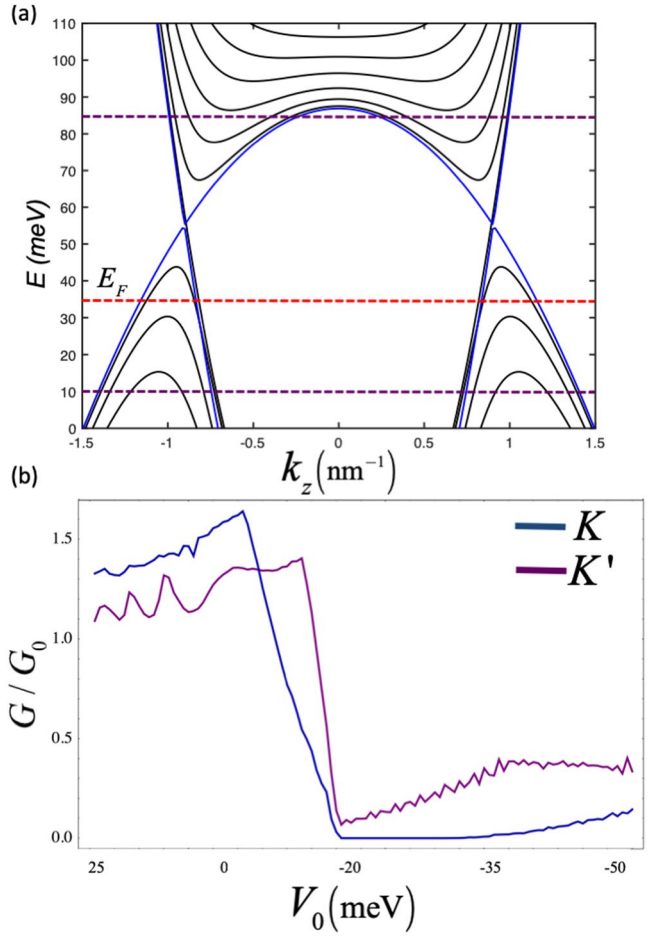

Figure 8. (**a**) The energy dispersion at $k_y = 0$, where the $E_F = 35\,\mathrm{meV}$ which is represented by the red dashed line. Two Weyl nodes appear at $k_z \simeq \pm 0.9\,\mathrm{nm}^{-1}$. In our model, the application of a top gate voltage generates electrostatic barrier height (V_0) in the central region. The conductance of the system shown in (**b**) is calculated for $-50\,\mathrm{meV} < V_0 < 25\,\mathrm{meV}$, which covers the applied potential range between the purple dashed lines. These lines indicate the levels in the central region where the Fermi level coincides with, in the case of $V_0 = 25\,\mathrm{meV}$ and $V_0 = -50\,\mathrm{meV}$. The material parameters used in the calculations are $C_0 = 0$, $C_1 = 67.538\,\mathrm{meV\,nm^2}$, $C_2 = -84.008\,\mathrm{meV\,nm^2}$, $M_0 = -86.86\,\mathrm{meV}$, $M_1 = -106.424\,\mathrm{meV\,nm^2}$, $M_2 = -103.610\,\mathrm{meV\,nm^2}$, $A = 245.98\,\mathrm{meV}$.

allowed for transmission (e.g. 100 meV in Fig. 4(c)). To implement the detector scheme, valley polarized transmission is generated at the first barrier by tuning the electrical potential of the proposed valley polarizer. Figure 9(a and b) shows two different configurations where the valley polarizer is set to the polarization of K and K' respectively. This can be achieved by tuning the electrical potential to -20 meV and 100 meV, which are the voltage values correspond to high polarization of K and K' respectively, based on the conductance profiles shown in Fig. 4. In the Fig. 9, the detector is set to measure K-polarization. The total transmission of the system clearly shows larger transmission when the incident current is K-polarized [see Fig. 9(c and d)]. To prove that the transmission difference originates from the valley polarization, we test the same barrier structures [Fig. 9(a and b)] in the case of ($w_y = 0$), where the two valleys are degenerate in k-space. For the given parameters, two different configurations produce almost the same transmission profile.

Existance of multiple pair of Weyl nodes. Since the number of Weyl nodes, their respective chirality and tilt direction can vary according to the host materials, we have focused on the simplest Weyl semimetal case where there exists only one pair of Weyl nodes related by inversion symmetry. The presented scheme is applicable to this form of Weyl semimetals which have been widely investigated[64–68]. To generalize our valley polarization study to the case of multiple pairs of Weyl nodes, we have to consider the fact that it is only the component of the tilt vector perpendicular to the transmission direction that is responsible for the valley-dependent angular separation at the barrier interfaces.

Based on this, we analyze the possible cases of Weyl semimetals depending on their chirality and tilt direction. The Weyl semimetal phase requires either broken inversion symmetry (a) or time reversal symmetry (b). One can basically analyze these cases as follows:

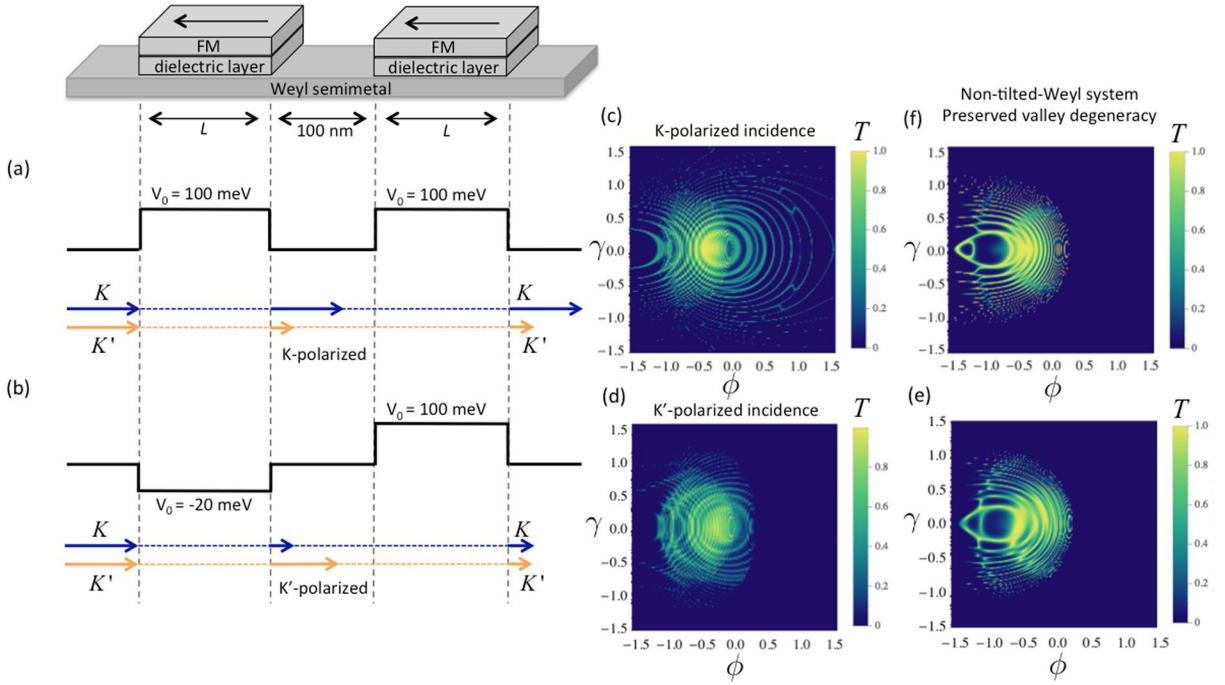

Figure 9. Detection scheme for valley polarization, which is comprised of serially connected valley filters. Each one is identical to the scheme shown in Fig. 1(a). The first barrier is used as polarizer, while the second barrier is used to detect generated valley polarization. (**a** and **b**) Shows two different configurations of the first barrier, i.e., set to the polarization of K and K' respectively. (**c** and **d**) Show the angular dependence of transmission probability of the system illustrated in (**a** and **b**) respectively. (**e** and **f**) Show the transmission probability for the valley-degenerate system ($w_y = 0$) in the case of the configurations shown in (**a** and **b**) respectively. The Fermi energy is 50 meV, barrier length $L = 900$ nm, magnetic field $B_0 = 2$ T for all configurations.

(a) If one Weyl node exists at K whose energy dispersion is described by $H = \hbar(v_F k.\ \sigma + w.\ k)$, another Weyl node must appear at $-K$ with opposite chirality due to the inversion symmetry, and its dispersion will be described by $H = \hbar(-v_F k.\ \sigma - w.\ k)$. Similarly, in the case of multiple pairs, as a result of inversion symmetry, Weyl nodes with different chiralities would possess tilt vectors in the opposite directions. In this case, the proposed filter serves a dual function, in that it would not only polarize the electrons according to their valley index, but also according to their respective chiralities.

(b) If one Weyl node is located at K described by $H = \hbar(v_F k.\ \sigma + w.\ k)$, the other Weyl node must appear at $-K$ related by time reversal symmetry, which may be described by $H = \hbar(v_F k.\ \sigma - w.\ k)$. In this case, there exists at least another pair of Weyl nodes in the Brillouin zone. However, in this case, further information such as the position of the Weyl nodes in k-space, their respective energy levels, must be accounted for in calculating the net valley polarization. These properties of the Weyl nodes is dependent on the crystal symmetries and material structure of the Weyl semimetal.

Therefore, we take the example of HgTe class materials to demonstrate the possible configuration that generates valley dependent conductance based on our approach. Recent works have shown that the HgTe class of materials host four pairs of Weyl nodes which are type-I or type-II according to the strength of the applied compressive strain[69]. By tuning the strain, the Weyl cones can be slightly tilted in the case of type-I, which is the case considered here.

Based on the Weyl node locations in HgTe shown in Fig. 10(a), the following points are important considerations for the possible experimental realization of the proposed valley filter.

(i) As the proposed approach is demonstrated by assuming ballistic tunneling transport, the Fermi surfaces around the Weyl nodes with different chirality must not be overlapping along k in the transmission direction. Otherwise, not only the momentum, but also the spin orientation in the vicinity of the valleys would influence the tunneling transmission. Although this may not totally suppress the valley dependent conductance, it may reduce the tunneling conductance due to the mismatch of the spin orientation. In this respect, HgTe is a suitable candidate for observing our proposed effect since there is no overlap between the valleys with different chiralities if one chooses the transmission direction to be along k_x or k_y or k_z as shown in Fig. 10(a–c).

(ii) The Weyl nodes with tilt vector pointing in opposite direction must not be overlapping along the transmission direction since the proposed method polarizes the valleys according to the tilt direction. HgTe would satisfy this under specific strain configuration that results in the ideal Weyl node distribution shown in Fig. 10, as discussed in ref.[69].

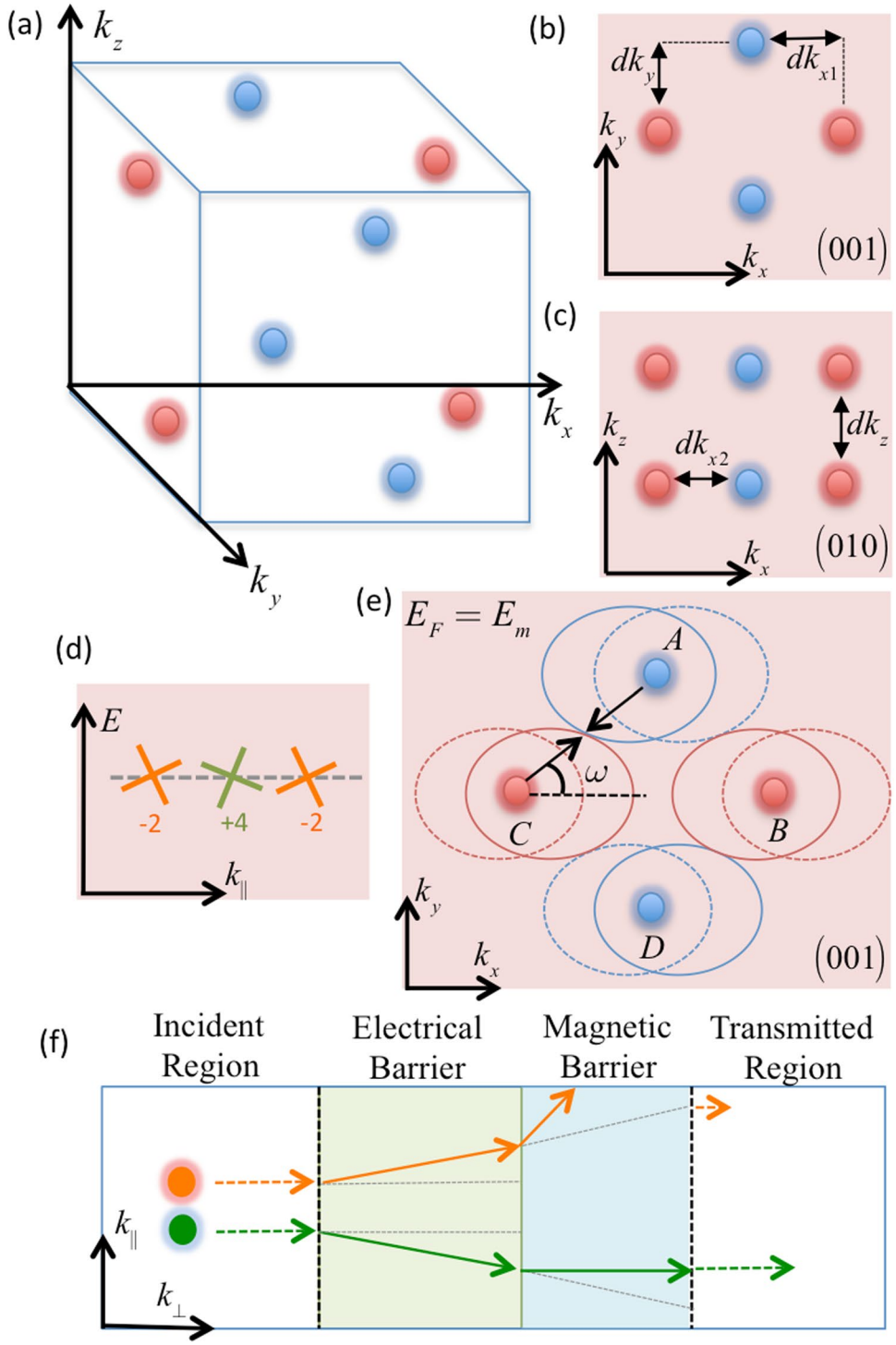

Figure 10. Weyl node configuration of HgTe under compressive strain that generate four pairs of type-I Weyl fermions, where the chirality of the Weyl nodes are represented by the red and blue colors. (**b** and **c**) Shows the reflection of the Weyl nodes on the (001) and (010) surface Brillouin zones. (**d**) Schematically illustrates the two groups of Weyl nodes classified according to their tilt directions. Each of the green and orange groups includes four Weyl nodes. (**e**) Shows the Fermi surface of the Weyl fermions, where the dashed-lined circle represents the Fermi surface of the same cone under electrical gate potential. The examplary configuration in (**e**) indicates the upper limit of the Fermi energy where there is no overlap between Fermi surfaces of different valleys. The proposed transport mechanisms is illustrated in (**f**), which effectively polarize, and filter the desired group of valleys [i.e., orange or green shown in (**d**)] by means of electrical and magnetic barriers. For simplicity, the magnetic and electrical barriers are illustrated sequantially., In the proposed model they operate simultaneously in the same barrier region.

(iii) The k-space distance of the Weyl nodes is a crucial factor due to the inter-valley scattering, which may reduce the valley polarization. However, the current Weyl semimetal candidates possess large enough k-space separation that effectively decouple the Fermi surfaces, and hence suppress the transmission between the valleys with opposite direction tilt. We analyze this in detail in a later section.

Consequently, based on the above analysis, the Weyl nodes can be characterized into two groups according to the direction of their tilt vector, and are represented by the green and orange cones in Fig. 10(d). Due to the opposite tilt direction of the nodes in the transverse direction, the electrons close to different valleys would experience a deflection in opposite directions according to their respective groups, as indicated by the green or orange arrows in Fig. 10(f). The transverse Lorentz displacement due to the magnetic barrier additionally deflects the electrons along the transverse direction, which results in valley dependent conductance across the barrier. In Fig. 10(f), for simplicity, the electric and magnetic barriers are illustrated sequentially. In actual fact, they are effective simultaneously in the same (central) region in the proposed model.

Based on the crystal structure of the materials, the two valley groups shown in Fig. 10(d and f) may be formed such that valleys in a group would share both the same tilt direction and chirality. In this case, our proposed model would yield electrons which are polarized according to the valley index, as well as chirality (i.e., they exhibit both valley and chirality polarization). This case occurs where tilt at a node is correlated with its chirality (e.g., the simplest Weyl semimetal phase with a single pair of nodes related by the inversion symmetry). We could also have the other scenario where valleys in each group only share the same tilt direction but not the chirality direction. In this case, our model would yield electrons which are only valley polarized. The detection scheme proposed in the manuscript (which is sensitive to the valley index) would be suitable for both cases. In the example of HgTe shown in Fig. 8, each orange and green group contains both chiralities (shown by blue and red). Thus the generated current would be polarized according to valley index, but not the chirality.

Consequently, even in such the case of multiple pairs of Weyl nodes, we would in general expect finite valley polarization to occur. Based on our proposed model, valleys that possess different tilt direction can be angularly separated with a single electrostatic barrier. Note that the tilt vectors of Weyl nodes does not need be exactly opposite to one another to allow valley polarization to occur. Valley polarization can be achieved as long as the transmission and tilt directions are not exactly parallel to each other. As a result, by choosing the transmission direction and the direction of the magnetic field according to the number and the position of the Weyl nodes, one can still generate valley-polarized transmission with multiple Weyl node pairs based on our proposed method.

k-space separation of the valleys. As mentioned earlier, the robustness of the Weyl semimetal case strongly depends on the k-space distance of the Weyl nodes, i.e., the length of the Fermi arc. The clustering of Weyl points close in k-space would negatively affect the valley polarization in the proposed scheme due to the inter-valley transmission of Weyl fermions. However, in terms of ballistic transport, intervalley transmission requires Fermi surface (FS) overlap due to the conservation of the transverse momentum. To investigate the effect of the Weyl node separation on the presented results, we consider the limiting case of the FSs where the overlap starts to occur between the propagating states of the different Weyl nodes (assuming low energy approximation). Since the Weyl node orientation in k-space depends on the crystal structure of the material, we focus on the specific HgTe example shown in Fig. 10. The four Weyl nodes located at $k_z = \pm k_z^*$ are perfectly overlapping along the choosen transmission direction k_z, which is a desirable condition as the momentum and the spin orientations are perfectly matched. The FS orientation is shown in Fig. 10(e), where the solid-lined circles represent the FSs out of the barrier region, and dashed-lined circles represent the FSs within the barrier region. In HgTe, the Weyl points are located at $(\pm k_x^*, 0, \pm k_z^*)$ and $(0, \pm k_y^*, \pm k_z^*)$ where $k_x^* = k_y^* = k^*$. Due the choice of transmission direction along k_z, transmission between different Weyl nodes would be excluded if there is no overlap of the FSs on the k_x-k_y plane. The limiting condition is shown in Fig. 10(e) where the FSs just touch each other with no overlap. Note that there is also relatively small momentum shift dk induced by the magnetic barrier (not visible in Fig. 10(e)), which shift the dashed-lined FSs further. To derive the analytical expression that describe the limitting condition, we consider without loss of generality on the specific Weyl node pair A and C [see Fig. 10(e)]. The touching point between the FSs of A and C can be found as $k_\omega = (E_m - V_0)/(\hbar(v_F + w_x\cos(\omega)))$, where ω is the angle shown in Fig. 10(e) which is given by $\omega = \tan^{-1}((k^*/(k^* + dk))$. And, the k-space distance between A and C is $\sqrt{(k^* + dk)^2 + (k^*)^2}$, which is also equal to $2k_\omega$. Thus, one can find the upper limit of the Fermi energy that avoids an overlap between FSs, which is given by

$$E_m = \frac{V_0}{2} + \frac{\hbar}{2}\left(v_F + \frac{w_x}{\xi}\right)\sqrt{(k^* + dk)^2 + (k^*)^2} \tag{16}$$

$$\xi = \sqrt{1 + \frac{(k^*)^2}{(k^* + dk)^2}} \tag{17}$$

In HgTe with the particular strain configuration, $k^* = 0.073\,\mathrm{nm}^{-1}$ (see ref.[69]) $E_m \simeq 22.5\,\mathrm{meV}$ in the case of the example configuration (i.e., consistent with the presented demonstration of the valley polarization) where $V_0 = 0\,\mathrm{meV}, dk \simeq -0.055\,\mathrm{nm}^{-1}, w_y = 0.4v_F$. We note that the inter-node separation can be much larger in other Weyl semimetals, e.g., in Ta_3S_2 it is as large as $1.5\,\mathrm{nm}^{-1}$ (see ref.[35]), which implies that the Fermi energy can be as large as $\simeq$496 meV without incurring overlap for the same configuration of dk, w_x, and V_0. These Fermi energy values are already higher or comparable to what we assume in our calculations. Furthermore, we note that the

proposed scheme does not impose a tight restriction on the Fermi energy. The system can operate over a wide range of Fermi energy by optimizing other parameters such as the magnetic field.

Conclusion

In summary, we presented a new type of valley filter approach that is compatible with all the systems containing tilted band structure. The presented effect originates from the coupling of the applied potential gradient and valley dependent tilt of energy dispersion around the Weyl points. Further investigation of this valley polarization effect may pave the way for novel applications in electron optics of Weyl semimetals. Valley-polarized tunneling applications have been proposed in many systems under the influence of uniaxial strain, such as in graphene and silicene, but modulation of the applied strain is not so straightforward. Unlike previous works, our analysis shows that the possibility of controlling valley-polarized tunneling by means of electrical bias in Weyl systems possessing tilted band structure, which is more readily achieved in practice. The parameters used in this work can be further optimized to achieve higher valley polarization.

References

1. Yao, W., Xiao, D. & Niu, Q. Valley-dependent optoelectronics from inversion symmetry breaking. *Physical Review B* **77**, 235406 (2008).
2. Xiao, D., Yao, W. & Niu, Q. Valley-Contrasting Physics in Graphene: Magnetic Moment and Topological Transport. *Physical Review Letters* **99**, 236809 (2007).
3. Akhmerov, A. R. & Beenakker, C. W. J. Detection of Valley Polarization in Graphene by a Superconducting Contact. *Physical Review Letters* **98**, 157003 (2007).
4. Rycerz, A., Tworzydlo, J. & Beenakker, C. W. J. Valley filter and valley valve in graphene. *Nat Phys* **3**, 172 (2007).
5. Shkolnikov, Y. P., De Poortere, E. P., Tutuc, E. & Shayegan, M. Valley Splitting of AlAs Two-Dimensional Electrons in a Perpendicular Magnetic Field. *Physical Review Letters* **89**, 226805 (2002).
6. Bishop, N. C. *et al*. Valley Polarization and Susceptibility of Composite Fermions around a Filling Factor $\nu = 3/2$. *Physical Review Letters* **98**, 266404 (2007).
7. Eng, K., McFarland, R. N. & Kane, B. E. Integer Quantum Hall Effect on a Six-Valley Hydrogen-Passivated Silicon (111) Surface. *Physical Review Letters* **99**, 016801 (2007).
8. Cai, T. *et al*. Magnetic control of the valley degree of freedom of massive Dirac fermions with application to transition metal dichalcogenides. *Physical Review B* **88**, 115140 (2013).
9. Gunlycke, D. & White, C. T. Graphene Valley Filter Using a Line Defect. *Physical Review Letters* **106**, 136806 (2011).
10. Mak, K. F., He, K., Shan, J. & Heinz, T. F. Control of valley polarization in monolayer MoS2 by optical helicity. *Nat Nano* **7**, 494 (2012).
11. Pereira, V. M. & Castro Neto, A. H. Strain Engineering of Graphene's Electronic Structure. *Physical Review Letters* **103**, 046801 (2009).
12. Fujita, T., Jalil, M. B. A. & Tan, S. G. Valley filter in strain engineered graphene. *Applied Physics Letters* **97**, 3 (2010).
13. Yesilyurt, C., Tan, S. G., Liang, G. & Jalil, M. B. A. Efficient dual spin-valley filter in strained silicene. *Applied Physics Express* **8** (2015).
14. Yesilyurt, C., Tan, S. G., Liang, G. C. & Jalil, M. B. A. Perfect valley filter in strained graphene with single barrier region. *Aip Advances* **6** (2016).
15. Zhai, F., Zhao, X., Chang, K. & Xu, H. Q. Magnetic barrier on strained graphene: A possible valley filter. *Physical Review B* **82**, 115442 (2010).
16. Zhai, F. & Chang, K. Valley filtering in graphene with a Dirac gap. *Physical Review B* **85**, 155415 (2012).
17. Cavalcante, L. S., Chaves, A., da Costa, D. R., Farias, G. A. & Peeters, F. M. All-strain based valley filter in graphene nanoribbons using snake states. *Physical Review B* **94**, 075432 (2016).
18. Moldovan, D., Ramezani Masir, M., Covaci, L. & Peeters, F. M. Resonant valley filtering of massive Dirac electrons. *Physical Review B* **86**, 115431 (2012).
19. Zhai, F. & Chang, K. Valley filtering in graphene with a Dirac gap. *Physical Review B* **85**, 155415 (2012).
20. Yesilyurt, C. *et al*. Anomalous tunneling characteristic of Weyl semimetals with tilted energy dispersion. *Applied Physics Letters* **111**, 063101 (2017).
21. Yesilyurt, C., Siu, Z. B., Tan, S. G., Liang, G. & Jalil, Mansoor B. A. Conductance modulation in Weyl semimetals with tilted energy dispersion without a band gap. *Journal of Applied Physics* **121**(24), 244303 (2017).
22. Huang, S. M. *et al*. A Weyl Fermion semimetal with surface Fermi arcs in the transition metal monopnictide TaAs class. *Nature Communications* **6** (2015).
23. Lv, B. Q. *et al*. Observation of Weyl nodes in TaAs. *Nature Physics* **11**, 724 (2015).
24. Volovik, G. E. Kopnin force and chiral anomaly. *Jetp Letters* **98**, 753 (2014).
25. Wan, X., Turner, A. M., Vishwanath, A. & Savrasov, S. Y. Topological semimetal and Fermi-arc surface states in the electronic structure of pyrochlore iridates. *Physical Review B* **83** (2011).
26. Weng, H. M., Fang, C., Fang, Z., Bernevig, B. A. & Dai, X. Weyl Semimetal Phase in Noncentrosymmetric Transition-Metal Monophosphides. *Physical Review X* **5** (2015).
27. Xu, S.-Y. *et al*. Discovery of a Weyl fermion semimetal and topological Fermi arcs. *Science* **349**, 613 (2015).
28. Siu, Z. B., Yesilyurt, C., Tan, S. G. & Jalil, M. B. Influence of Fermi arc states and double Weyl node on tunneling in a Dirac semimetal. *Scientific Reports* **7**, 4030 (2016).
29. Li, S., Andreev, A. V. & Spivak, B. Z. Klein tunneling and magnetoresistance of p–n junctions in Weyl semimetals. *Physical Review B* **94**, 081408 (2016).
30. You, W. L., Wang, X. F., Oles, A. M. & Zhou, J. J. Electronic properties in a quantum well structure of Weyl semimetal. *Applied Physics Letters* **108**, 4 (2016).
31. Bai, C. X., Yang, Y. L. & Chang, K. A statistical algorithm showing coenzyme Q10 and citrate synthase as biomarkers for mitochondrial respiratory chain enzyme activities. *Scientific Reports* **6**, 15 (2016).
32. Yang, S. A., Pan, H. & Zhang, F. Chirality-Dependent Hall Effect in Weyl Semimetals. *Physical Review Letters* **115**, https://doi.org/10.1103/PhysRevLett.115.156603 (2015).
33. Jiang, Q.-D., Jiang, H., Liu, H., Sun, Q.-F. & Xie, X. C. Topological Imbert-Fedorov Shift in Weyl Semimetals. *Physical Review Letters* **115**, 156602 (2015).
34. Chang, T.-R. *et al*. Prediction of an arc-tunable Weyl Fermion metallic state in $Mo_xW_{1-x}Te_2$. *Nat Commun* **7** (2016).
35. Chang, G. Q. *et al*. A strongly robust type II Weyl fermion semimetal state in Ta_3S_2. *Science Advances* **2**, 8 (2016).
36. Liu, Y. *et al*. Gate-tunable quantum oscillations in ambipolar Cd_3As_2 thin films. *Npg Asia Materials* **7** (2015).
37. Liu, Z. K. *et al*. A stable three-dimensional topological Dirac semimetal Cd_3As_2. *Nature Materials* **13**, 677 (2014).
38. Wang, Y. *et al*. Gate-tunable negative longitudinal magnetoresistance in the predicted type-II Weyl semimetal WTe_2. *Nature Communications* **7**, 13142 (2016).

39. Yesilyurt, C., Tan, S. G., Liang, G. & Jalil, M. B. A. Klein tunneling in Weyl semimetals under the influence of magnetic field. *Scientific Reports* **6**, 38862 (2016).
40. Zhai, F. & Chang, K. Theory of huge tunneling magnetoresistance in graphene. *Physical Review B* **77**, 113409 (2008).
41. Wu, Z., Peeters, F. M. & Chang, K. Electron tunneling through double magnetic barriers on the surface of a topological insulator. *Physical Review B* **82**, 115211 (2010).
42. Cerchez, M., Hugger, S., Heinzel, T. & Schulz, N. Effect of edge transmission and elastic scattering on the resistance of magnetic barriers: Experiment and theory. *Physical Review B* **75**, 035341 (2007).
43. Hong, J. *et al*. Local Hall effect in hybrid ferromagnetic/semiconductor devices. *Applied Physics Letters* **90**, 023510 (2007).
44. Kubrak, V. *et al*. Magnetoresistance of a two-dimensional electron gas due to a single magnetic barrier and its use for nanomagnetometry. *Applied Physics Letters* **74**, 2507 (1999).
45. Matulis, A., Peeters, F. M. & Vasilopoulos, P. Wave-vector-dependent tunneling through magnetic barriers. *Physical Review Letters* **72**, 1518 (1994).
46. Nogaret, A., Bending, S. J. & Henini, M. Resistance Resonance Effects through Magnetic Edge States. *Physical Review Letters* **84**, 2231 (2000).
47. Nogaret, A., Lawton, D. N., Maude, D. K., Portal, J. C. & Henini, M. Hall anomaly of diffusive magnetic waveguides. *Physical Review B* **67**, 165317 (2003).
48. Vančura, T. *et al*. Electron transport in a two-dimensional electron gas with magnetic barriers. *Physical Review B* **62**, 5074 (2000).
49. Bending, S. J., von Klitzing, K. & Ploog, K. Weak localization in a distribution of magnetic flux tubes. *Physical Review Letters* **65**, 1060 (1990).
50. Carmona, H. A. *et al*. Two Dimensional Electrons in a Lateral Magnetic Superlattice. *Physical Review Letters* **74**, 3009 (1995).
51. Datta, S. *Electronic Transport in Mesoscopic Systems*, Cambridge Studies in Semiconductor Physics and Microelectronic Engineering (Cambridge University Press, Cambridge, 1995).
52. Gökemeijer, N. J., Ambrose, T. & Chien, C. L. Long-Range Exchange Bias across a Spacer Layer. *Phys. Rev. Lett*. **79**, 4270 (1997).
53. Cheng, L. *et al*. Pd polarization and interfacial moments in Pd-Fe multilayers. *Phys. Rev. B* **69**, 144403 (2004).
54. Lim, W. L., Ebrahim-Zadeh, N., Owens, J. C., Hentschel, H. G. E. & Urazhdin, S. Temperature-dependent proximity magnetism in Pt. *Applied Physics Letters* **102**, 162404 (2013).
55. Fatemi, V. *et al*. Magnetoresistance and quantum oscillations of an electrostatically tuned semimetal-tometal transition in ultrathin WTe_2. *Physical Review B* **95**, 041410 (2017).
56. Xiao, X., Yang, S. A., Liu, Z., Li, H. & Zhou, G. Anisotropic Quantum Confinement Effect and Electric Control of Surface States in Dirac Semimetal Nanostructures. *Scientific Reports* **5**, 7898 (2015).
57. Pan, H., Wu, M., Liu, Y. & Yang, S. A. Electric control of topological phase transitions in Dirac semimetal thin films. *Scientific Reports* **5**, 14639 (2015).
58. Wang, Z., Weng, H., Wu, Q., Dai, X. & Fang, Z. Three-dimensional Dirac semimetal and quantum transport in Cd_3As_2. *Physical Review B* **88**, 125427 (2013).
59. Wang, Z. *et al*. Dirac semimetal and topological phase transitions in A_3Bi (A = Na, K, Rb). *Physical Review B* **85**, 195320 (2012).
60. Shimazaki, Y. *et al*. Generation and detection of pure valley current by electrically induced Berry curvature in bilayer graphene. *Nat Phys* **11**, 1032 (2015).
61. Sui, M. *et al*. Gate-tunable topological valley transport in bilayer graphene. *Nat Phys* **11**, 1027 (2015).
62. Akhmerov, A. R. & Beenakker, C. W. J. Detection of Valley Polarization in Graphene by a Superconducting Contact. *Physical Review Letters* **98**, 157003 (2007).
63. Wu, Z., Zhai, F., Peeters, F. M., Xu, H. Q. & Chang, K. Valley-Dependent Brewster Angles and Goos-Hänchen Effect in Strained Graphene. *Physical Review Letters* **106**, 176802 (2011).
64. Burkov, A. A. & Balents, L. Weyl Semimetal in a Topological Insulator Multilayer. *Physical Review Letters* **107**, 127205 (2011).
65. Yang, S. A., Pan, H. & Zhang, F. Chirality-Dependent Hall Effect in Weyl Semimetals. *Physical Review Letters* **115** (2015).
66. McCormick, T. M., Kimchi, I. & Trivedi, N. Minimal models for topological Weyl semimetals. *Physical Review B* **95**, 075133 (2017).
67. Wang, Z. *et al*. Time-Reversal-Breaking Weyl Fermions in Magnetic Heusler Alloys. *Physical Review Letters* **117**, 236401 (2016).
68. Liu, C.-X., Ye, P. & Qi, X.-L. Chiral gauge field and axial anomaly in a Weyl semimetal. *Physical Review B* **87**, 235306 (2013).
69. Ruan, J. *et al*. Symmetry-protected ideal Weyl semimetal in HgTe-class materials. *Nature Communications* **7**, 11136 (2016).

Acknowledgements

The authors would like to acknowledge the MOE Tier II grant MOE2013-T2-2-125 (NUS Grant No. R-263-000-B10-112), and the National Research Foundation of Singapore under the CRP Program "Next Generation Spin Torque Memories: From Fundamental Physics to Applications" NRF-CRP9-2013-01, and the MOE-AcRF Tier-II grant MOE2015-T2-1-099 (NUS Grant No. R-380-000-012-112) for financial support.

Author Contributions

C.Y. developed the idea and performed analytical and theoretical calculations. Z.B.S. performed numerical calculations. The obtained results were discussed with S.G.T., G.L., S.A.Y., and M.B.A.J. C.Y. and M.B.A.J. wrote the manuscript. All the authors contributed to the interpretation and discussion of obtained results and commented on the manuscript.

Additional Information

Competing Interests: The authors declare no competing interests.

Publisher's note: Springer Nature remains neutral with regard to jurisdictional claims in published maps and institutional affiliations.